Meqbel, N., Ritter, O., DESIRE Group (2013): A magnetotelluric transect across the Dead Sea Basin: electrical properties of geological and hydrological units of the upper crust. - Geophysical Journal International, 193, 3, pp. 1415—1431.

DOI: http://doi.org/10.1093/gji/ggt051

Geophysical Journal International

Geophys. J. Int. (2013) **193,** 1415–1431
Advance Access publication 2013 March 08

doi: 10.1093/gji/ggt051

A magnetotelluric transect across the Dead Sea Basin: electrical properties of geological and hydrological units of the upper crust

Naser M. M. Meqbel, Oliver Ritter and DESIRE Group

German Research Centre For Geosciences, GFZ-Potsdam, Department 2/Section 2.2 *Geophysical Deep Sounding Telegrafenberg,* 14473 *Potsdam, Germany. E-mail: meqbel@gfz-potsdam.de*

Accepted 2013 February 5. Received 2013 February 4; in original form 2012 May 31

SUMMARY

Oblique shear directions along the left lateral strike-slip Dead Sea transform (DST) fault caused the formation of the Dead Sea Basin (DSB), one of the world's largest pull-apart basins. The Dead Sea, which covers the northern part of the basin, is one of the most saline lakes in world. To understand interaction of saline water from the Dead Sea with the neighbouring hydrological system is an important geoscientific problem for this arid region. Here, we report on the first continuous magnetotelluric (MT) transect crossing the entire DSB, from the eastern to the western rift shoulders and beyond. 2-D inversion of the MT data reveals an unprecedented comprehensive picture of the subsurface structures from the basin and adjacent areas. Quaternary to recent sediments of the Al-Lisan/Samara formations are expressed as highly conductive structures reaching a depth of approximately 4 km. East and west of the rift valley layered sequences of resistive and conductive structures coincide with the sedimentary formations of the Cretaceous, Jurassic and Triassic. Pre-Cambrian basement (crystalized igneous rocks) appears at depths >3 km beneath both rift shoulders as very resistive regions. The eastern boundary fault of the DST is associated with a sharp lateral conductivity contrast between the highly resistive basement structures and the conductive fill of the DSB. The transition to the western rift shoulder appears wider and smoother, in agreement with a broader fractured region, possibly caused by a combination of strong normal faulting and strike-slip activity. The very high conductivities of less than 1 Ωm of the Al-Lisan/Samara formations can be explained with hypersaline waters of the Dead Sea reaching depths of a few kilometres and porosities of at least 37 per cent. The regional Judea and Kurnub aquifers of the Cretaceous are imaged as conductive layers with resistivities of 1–20 Ωm and we infer porosities of 15 per cent. The low resistivities observed in the Jurassic/Triassic formations can be explained with highly saline or saturated brines and a porosity of 7 per cent. From the electrical conductivity images and estimating porosities of the sedimentary rocks, we can infer salinities of the various aquifers. For the Al-Lisan/Samara formations, salinities reach values >50 g l^{-1} in the upper 1.7 km. The Judea, Kurnub and Jurassic/Triassic aquifers have a more inhomogeneous distribution of salinity with highest values observed between normal faults at the western rift shoulder.

Key words: Magnetotelluric; Hydrogeophysics; Transform faults.

1 INTRODUCTION

Electromagnetic (EM) methods are used to image the electrical conductivity distribution of the subsurface. The exploration depth of the EM methods varies between a few tens of metres to several hundreds of kilometres. EM methods are therefore routinely applied in shallow environmental studies as well as in deep geodynamic studies. Active source EM methods [e.g. controlled-source EM (CSEM) and time domain EM (TDEM)] have been used to delineate the spatial distribution of groundwater aquifers and hydrocarbonate reservoirs (Kafri *et al.* 1997; Levi *et al.* 2008; Constable 2010). The magnetotelluric (MT) method is often applied to image the Earth's crust and upper mantle. However, with dense station coverage and short-period data the MT method can also be used to unravel shallow structures.

The MT method was a main component in the multidisciplinary multinational DESIRE project (Dead Sea Integrated REsearch). The main objectives of the DESIRE project are to study geodynamic processes controlling the evolution of the Dead Sea Basin (DSB) and the tectonic setting. In addition, the architecture and composition of

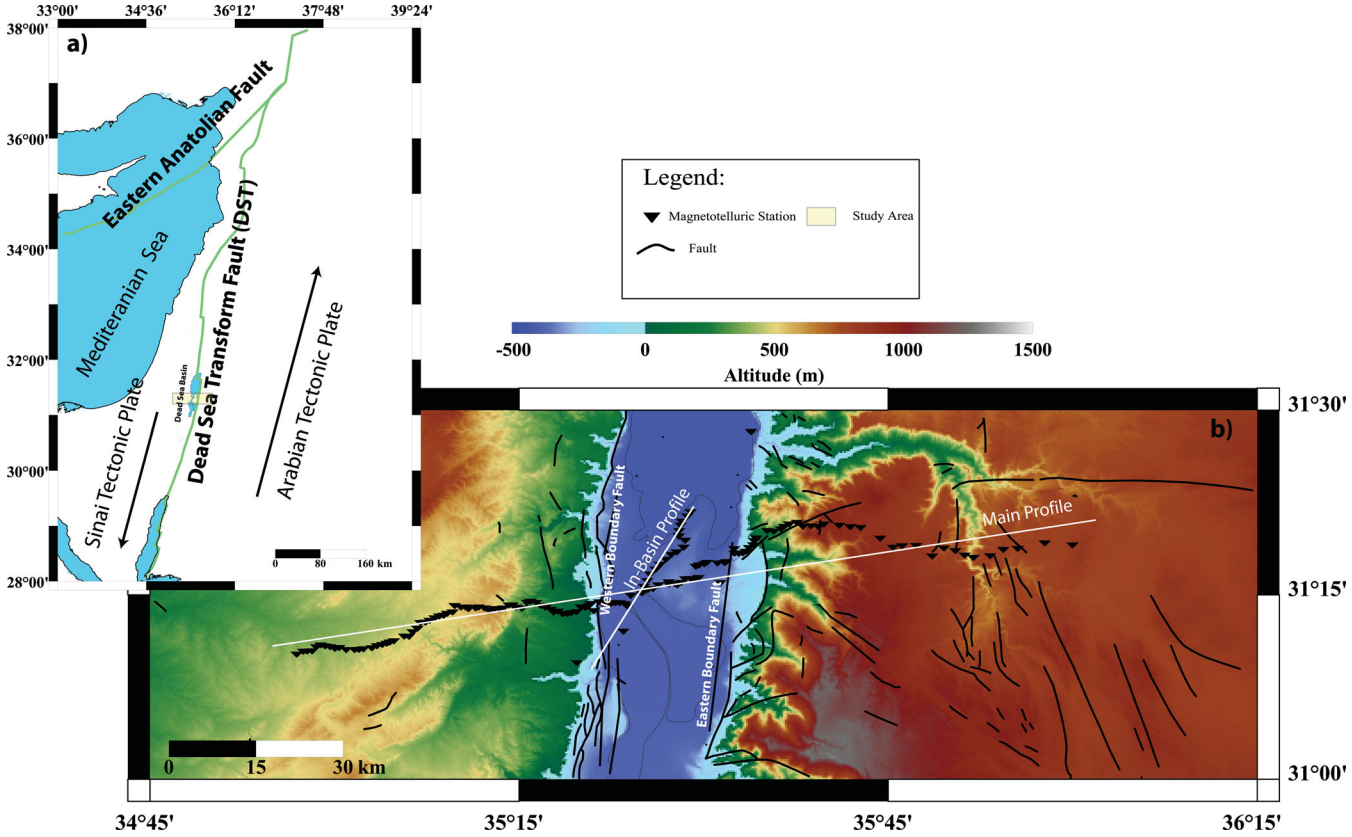

Figure 1. (a) The Dead Sea transform (DST) fault separates the Arabian tectonic plate in the east from the Sinai and African plates in the west. The Dead Sea Basin (DSB) was formed due to oblique shear directions along the DST. (b) Topographic map with the locations of the MT stations along the main and the In-Basin profiles (white lines). Black triangles indicate locations of MT broad-band (BB) stations. Main faults in the vicinity of the Dead Sea Basin are plotted as black lines. The DSB is delimited by the Eastern Boundary Fault (EBF) and the Western Boundary Fault at the eastern and western margins, respectively.

the shallow DSB, particularly the depth of the sedimentary basin, are key questions of the project.

The DSB was formed as a result of the late Cenozoic breakup of the Arabo-African Plate along the Dead Sea Transform (DST; Garfunkel & Ben-Avraham 1996). The DST is a left-lateral strike-slip transform fault separating the African and Sinai plates in the west from the Arabian Plate in the east (Fig. 1a). The oblique shear directions of the DST caused the formation of several pull-apart basins. The largest pull-apart basin along the DST, and probably on Earth, is the DSB. Garfunkel & Ben-Avraham (1996) suggested a connection between the DSB and the Mediterranean Sea in the Late Miocene and Pliocene. This connection resulted in the deposition of large volumes of marine sediments, such as Halite (Sedom formation). Uplift along the transform fault(s) delimiting the DSB in the Late Miocene cut off the connection to the Mediterranean Sea and a saline lake (Al-Lisan Lake) formed in the topographic low (Garfunkel & Ben-Avraham 1996).

The DSB is approximately 150 km long and extends from the Jordan Valley in the north to the central Araba Valley in the south. The northern part of the basin is mostly covered by the Dead Sea brines, forming one of the most saline lakes in the world. The salinity of the Dead Sea brines (340 g l^{-1} TDS; total dissolved solid) is 10 times higher than the salinity of sea water (Ezersky *et al.* 2011). The invasion of the saline water body of the Dead Sea into deep aquifers at the eastern and western rift shoulders and its interaction with adjacent shallow freshwater aquifers are important topics for geophysical and hydrological studies. A palaeohydrological simulation by Stanislavsky & Gvirtzman (1999) suggested that Dead Sea brines started to migrate laterally and invaded the adjacent shallow and deep aquifers over the last 2 Ma. With continuing uplifting of the rift shoulders' shallow aquifers were flushed with meteoric water. This fresh water flows from the rift shoulders downwards into the rift valley while brines of the deeper aquifers are unaffected. This scenario is supported by salinity values measured in deep boreholes at the western rift shoulder (Fleischer *et al.* 1977).

Several regional aquifers dominate the hydrological system in the study area. At the eastern and western rift shoulders, the main aquifers are the Ajloun/Judea and the Kurnub formations of the upper and lower Cretaceous, respectively (Stanislavsky & Gvirtzman 1999; Gvirtzman & Stanislavsky 2000; Salameh & El-Naser 2000; Ben-Itzhak & Gvirtzman 2005; Kafri & Goldman 2005; Eraifej 2006; Yechieli 2006). Additional deep aquifers of Jurassic, Triassic and Cambrian age were reported by Stanislavsky & Gvirtzman (1999) for the western rift shoulder and by Khalil (1992) for the eastern rift shoulder. In the central part of the DSB, an alluvial Quaternary aquifer which is delimited by a normal fault system in the west and by strike-slip faults in the east is the shallowest aquifer in the study area (the DS Coastal aquifer).

Geophysical methods have been routinely applied to detect the fresh/saline water interface along the eastern and western shore lines of the Dead Sea. Using DC-Geoelectric and TDEM methods Salameh & El-Naser (2000), Kafri *et al.* (1997), Yechieli *et al.* (2001), Yechieli (2006) and Kafri & Goldman (2005) concluded that electrical resistivity values below 1 Ωm are typical for intruded brines. Moreover, these authors showed that the fresh/saline water interface is about nine times shallower in the vicinity of the Dead Sea

than for normal sea water conditions. A study delineating the spatial distribution of groundwater salinity at the western rift shoulder using TDEM methods by Levi *et al.* (2008) showed a heterogeneous salinity distribution for the Judea aquifer.

TDEM and DC methods are generally limited in their sounding depths to the upper few hundred metres, although Levi *et al.* (2008) discussed structures as deep as 1600 m. Therefore, most previous studies concentrated on characterizing the shallow Ajloun/Judea and underlying Kurnub aquifers without reaching the base of the Kurnub. Electrical or EM studies of the deeper Jurassic, Triassic and Cambrian aquifers have not been conducted. Interpretation of the existing TDEM data is mostly based on 1-D modelling, which can be inadequate in the presence of strong lateral conductivity variations.

Our MT transect crosses for the first time the entire DSB, from the eastern to the western rift shoulders and beyond. The results presented here, show an unprecedented comprehensive picture of the subsurface electrical conductivity distribution within the basin and adjacent areas. With dense station spacing and broad-band (BB) frequency range of the MT data we can shed light on the entire geological and hydrological system of the region, including shallow as well as deep aquifers at the eastern and western rift shoulders. The interpretation is based on 2-D inversion which resolves vertical and lateral conductivity contrasts.

2 METHOD, EXPERIMENT DESIGN AND DATA EVALUATION

The MT method relies on naturally occurring EM field variations generated in the ionosphere and by lighting discharges, which induce currents into the Earth. The theory behind the method has been described before, for example, Cagniard (1953), Keller (1988) and Weaver (1994). Field data are acquired by measuring variations of electric (**E**) and magnetic (**B**) fields at Earth's surface, typically using non-polarizing electrodes and induction coil magnetometers. The magnetic field components B_x, B_y and B_z are oriented in N–S, E–W and vertical directions, and the two horizontal electric dipoles E_x and E_y are oriented in N–S and E–W directions. From the recorded time-series of the horizontal electric and magnetic fields, the so-called impedance tensor (**Z**) is calculated. The impedance tensor depends on frequency (or period) and is usually presented as apparent resistivity and phase.

The DESIRE-MT data were collected in 2006 October and November. The measurements were carried out along two profiles (see Fig. 1 b). The main profile is oriented N70°E, approximately perpendicular to the surface trace of the DST with a length of approximately 110 km. A second, approximately 20 km long (In-Basin) profile is oriented N20°E in parallel to the western shore of the Al-Lisan Peninsula. In this study, we report on results obtained from the main profile.

In total, 153 MT stations (94 and 59 along the main and short profiles, respectively) were deployed with a site spacing varying between 0.5 and 2 km. In the DSB and its vicinity, the spacing was 0.5 km, further away from the DSB and towards the outer segments of the profile, the distances between the stations increased to 2 km. Short-period automatic magnetotelluric systems (Ritter *et al.* 1998, S.P.A.M. MkIII) and Earth Data Logger instruments were used to record data in the frequency range from 1 kHz to 1 mHz. At all stations, induction coil magnetometers (Metronix MFS05/6) were used to record three orthogonal magnetic field components. The total recording time for each of these BB stations 3 days. We used our own non-polarizing silver/silver chloride electrodes for all measurements.

Data acquisition was accomplished with two independent teams, working at the same time in Jordan and Israel which allowed us to operate up to 30 instruments recording simultaneously. This provided great flexibility to use remote reference (RR) processing with many combinations of sites. The recorded time-series were processed using the EMERALD package (Ritter *et al.* 1998; Weckmann *et al.* 2005; Krings 2007) to estimate impedance tensor and vertical magnetic transfer functions. Initially, the data were subjected to single-site (SS) processing using only electric and magnetic field components of a local site. EM noise (i.e. power lines) affects the SS estimated transfer functions considerably in the period range between 1 and 10 s (dead band). For the RR processing technique, horizontal magnetic field components of the local site are used together with the magnetic field components of a remote site (Gamble *et al.* 1979; Egbert 1997). The quality of the data around 10 s improved considerably after applying the RR processing technique.

2.1 Strike direction and dimensionality analysis

A quantitative determination of the regional geoelectric strike direction can be derived from the impedance tensor (**Z**), with so-called tensor decomposition methods. The method described by Becken & Burkhardt (2004) to estimate the geoelectric strike direction is based on an ellipse parametrization of the impedance tensor columns. The ellipticities of the impedance tensor columns are rotationally variant parameters. They vanish for 2-D EM field conditions if the data are rotated to the regional strike direction. Therefore, the regional strike direction can be determined by minimizing the sum of squared ellipticities weighted with their variances by rotating the coordinate system. The minimisation procedure can be applied for individual periods and sites as well as for a range of periods and/or sites.

Fig. 2(a) summarizes the geoelectric strike direction estimates. The MT stations are subdivided into three distinct groups: Western and eastern stations with more stable regional geoelectric strike direction between 10° and 15° reflecting predominantly 2-D conditions. Stations located in the DSB show strong variation in the strike direction values. This reflects the complexity of the geological and tectonic setting of the DSB and consequently the measured EM fields in this area. Nevertheless, for these stations and in the period range 1–1000 s one can still recognize predominately N–S-oriented strike directions.

The skew parameter is an indicator for the dimensionality structure of the subsurface and the associated EM fields (e.g. Vozoff 1972; Bahr 1988). In the original approach, the skew was calculated as the magnitude of the complex ratio between the main diagonal and the off-diagonal elements of the impedance tensor (e.g. Vozoff 1972). For ideal 1-D or 2-D structures, the value of the skew is zero. For 3-D structures, skew values of 1 and above have been observed. Bahr (1988) suggested an empirical threshold value of 0.3 above which the observed EM fields are inconsistent with 1-D or 2-D conditions.

Fig. 2(b) shows a summary of skew values for all sites of the main profile as a function of period. Skew values <0.3 are observed for periods <8 s. A gradual increase to values >0.3 is observed for periods >8 s. Fig. 2(b) shows that MT data at longer periods (>8 s) are affected by 3-D structures. To examine which stations are most severely affected by 3-D structures the skews are presented in Fig. 2(c) as a function of station position along the main profile for periods longer than 1 s. Obviously, most of the stations located to the west and to the east of the DSB have skew values less or

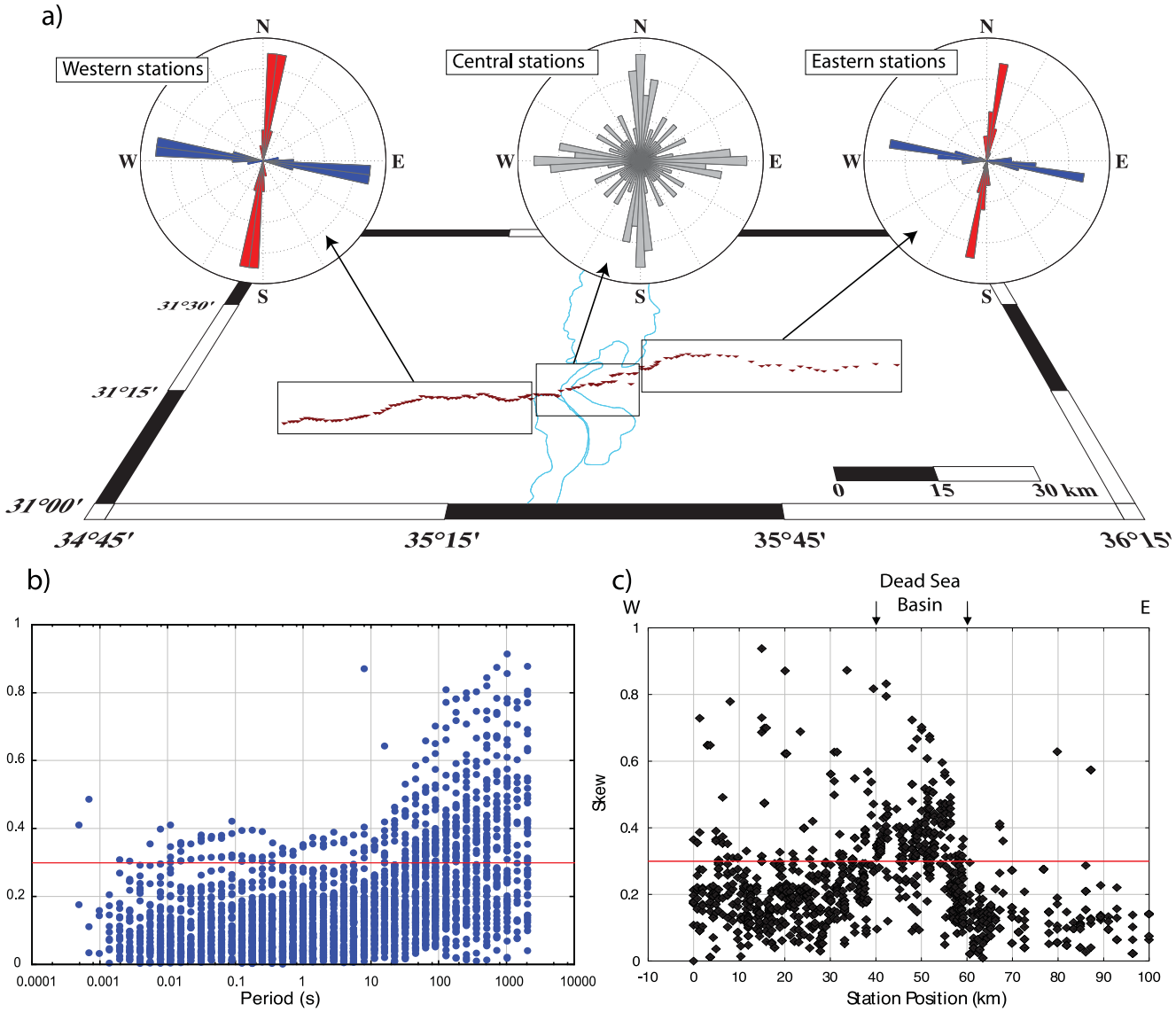

Figure 2. (a) Strike directions computed using the method described by Becken & Burkhardt (2004) in the period range from 1 to 1000 s for different segments of the main profile. The rose diagrams of strike direction at the western and eastern segments indicate a dominant N–S strike direction. Strike directions at central stations show greater variation but a predominant N–S direction can still be recognized. Sectors of the rose diagram marked in blue show a 90° ambiguity of the calculated strike direction. (b) Skew values presented as a function of periods indicate that the MT data at long periods (>8 s) are affected by 3-D structures. (c) Skew values along the main profile confirm that impedances on the eastern and western rift shoulders are compatible with 2-D structures, whereas, the central part is influenced by 3-D subsurface structures.

equal to 0.2. In the central part of the profile, skew values are often significantly higher than 0.3. This observation agrees with the result obtained from the geoelectric strike direction analysis: Data from stations in the east and west have a predominantly 2-D nature with a stable geoelectric strike direction between 10° and 15° and skew values below 0.2. Whereas, data from stations located within the DSB show a greater variety of geoelectric strike directions and skew values >0.3.

By rotating the impedance tensor into the geoelectrical regional strike direction of 12°, the data are assigned to the E- and B-polarizations. For the E-polarization (TE-mode), electric currents flow parallel to the strike direction. Electric currents of the B-polarization (TM-mode) flow perpendicular to the strike. Multisite, multiperiod data sets are commonly presented as pseudo-sections of apparent resistivities and phases for both TE- and TM-modes (Figs 3a and b). The most obvious features in the pseudo-sections are very low apparent resistivity values (<1 Ωm) for stations in the DSB (label A in Figs 3a and b). In the TE-mode, this feature covers the period range from 0.001 to 50 s. Low TM-mode apparent resistivity values, however, are also be observed at stations in the westernmost part of the DSB with corresponding high phase values of 70°. The apparent resistivity values for the TE-mode at longer periods (>10 s) do not indicate the same behaviour as in the TM-mode (label B in Figs 3a and b). Instead, the apparent resistivity values vary between 10 and 100 Ωm with phases at longer period (>10 s) just above 45°. This difference between TM- and TE-modes at longer periods indicates 2-D or more complicated structures at depth. Stations located in the DSB indicate another interesting feature. At periods between 1 and 10 s, an increase in the apparent resistivity values is observed (label C). The corresponding phases show low values of 10° for the TM-mode and around 20° for the TE-mode. This spatially localized feature indicates a resistive

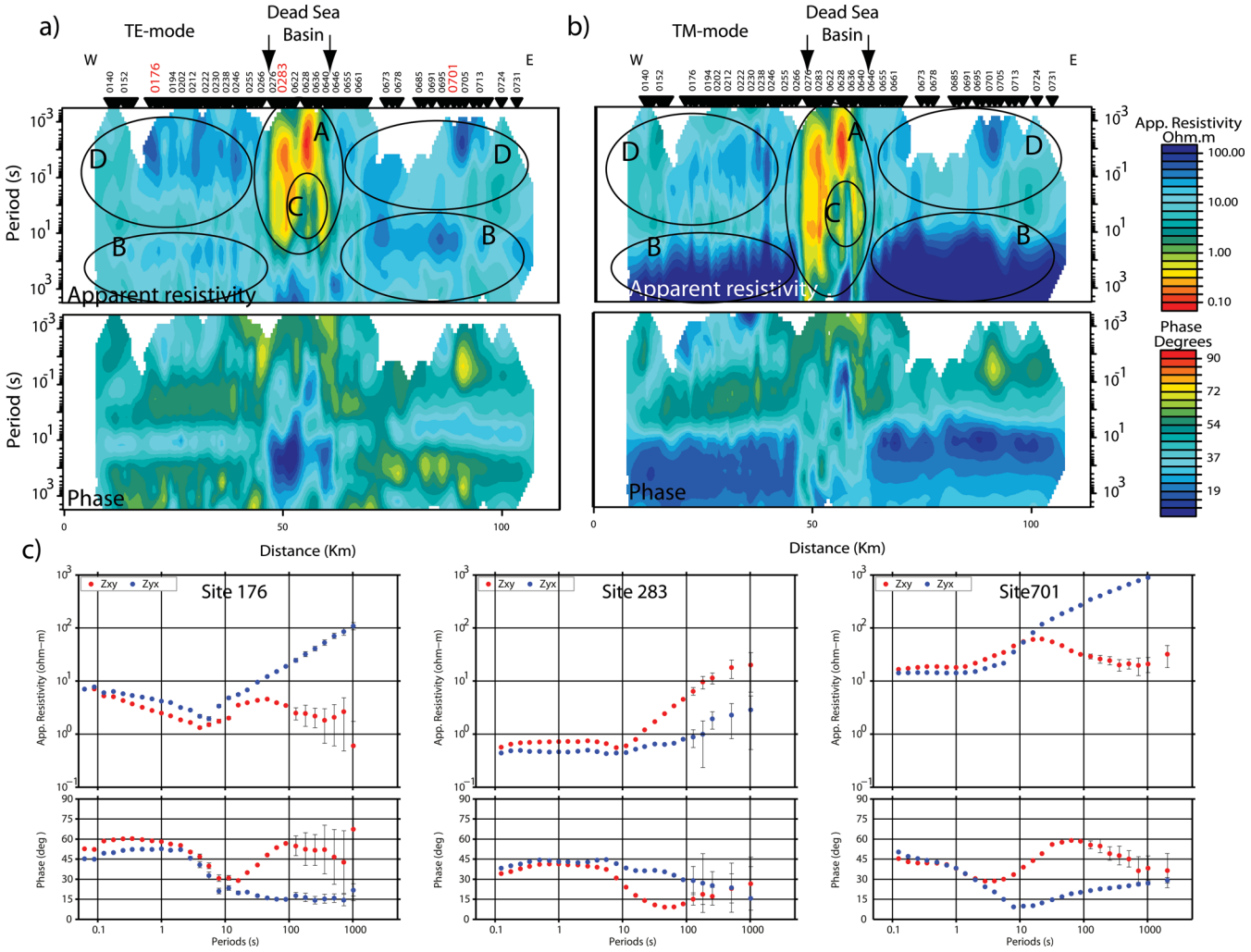

Figure 3. Pseudo-sections of apparent resistivity (upper panels) and phases (lower panels) for (a) TE-mode and (b) TM-mode along the main profile. Low apparent resistivity values (<1 Ωm) are observed at stations located in the Dead Sea Basin. Data from stations located to the east and west of the Dead Sea Basin show a split between TE- and TM-mode at periods around 10 s. The TM-mode apparent resistivity values increase and reach values higher than 100 Ωm at periods >1000 s, while the corresponding TM-mode phases decrease to <10°. Letters A, B, C and D denote areas with similar apparent resistivity and phase characteristics between the TE and TM-modes (see text for further explanation). (c) Apparent resistivity and phase curves of three selected sites (labelled in red in (a) from the western and eastern rift shoulders (sites 176 and 701) and the Dead Sea Basin (site 283). Smoothly varying curves generally indicate good data quality. Most prominent is a drop in the general levels of the apparent resistivity curves to values below 1 Ωm for stations located in the Dead Sea Basin.

structure embedded in a highly conductive host. Data of stations located to the east and west of the DSB and for periods <10 s are consistent with a 1-D or 2-D nature of the shallow subsurface (label D). Fig. 3(c) shows apparent resistivity and phase curves of three selected sites from the western and eastern rift shoulders (sites 176 and 701, respectively) and from the DSB (site 283). Smoothly varying curves generally indicate good data quality. Most prominent is the drop in the general levels of the apparent resistivity curves to values below 1 Ωm for stations located in the DSB.

3 TWO-DIMENSIONAL INVERSION

For 2-D inversion, we used the regularized non-linear conjugate gradient (NLCG) algorithm described by Rodi & Mackie (2001). This algorithm is implemented in the WINGLINK software package (software version 2.20.10; http://www.geosystem.net). The numerical algorithm described by Rodi & Mackie (2001) is based on a finite differences (FD) scheme. To obtain an accurate solution of Maxwell's equations, the Earth's subsurface is subdivided in small rectangular cells. In the course of the inversion, the NLCG algorithm assigns conductivity values to each cell in the attempt to fit the measured data. Our 2-D earth model for the DSB is discretized into 248 and 127 cells in horizontal and vertical directions, respectively. The width of cells is almost linear in the area of interest with an average width of ∼300 m. With greater distance from the area of interest the cell widths increase logarithmically to avoid an influence from the model boundaries. The cell thicknesses in the upper 5 km of the model were chosen to be very small (20 m for the first layer and logarithmically increasing with a factor of 1.1) to ensure accurate solution of the differential equations for the high-frequency data. Fine vertical gridding is also required to recover shallow structures. We also included topography to simulate more realistic earth models. The entire model domain extends from −10 000 to 10 000 km in horizontal directions and to a depth of 3500 km in the vertical direction. These large distances are necessary to avoid boundaries effect.

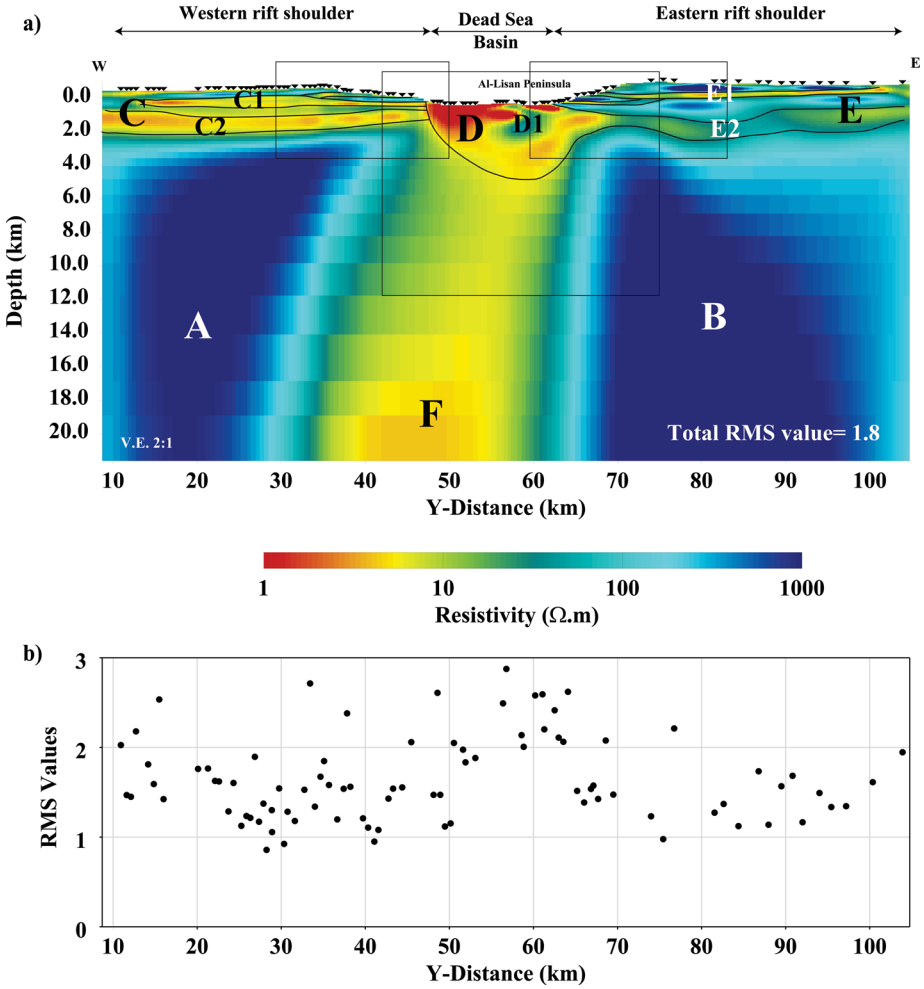

Figure 4. (a) Preferred 2-D conductivity model showing the most robust structures to a depth of ∼20 km. A and B are two resistive blocks which begin at a depth of ∼2.5 km. They are separated by the central conductive part of the model (label F). C describes a resistive–conductive sequence in the west which contains the two conductive layers C1 and C2. D is an extremely conductive feature which spans the central segment of the model and extends to a depth of ∼3 km. D is interrupted by resistive block D1 which extends to a depth of ∼2.5 km. E is a resistive-conductive sequence in the east which contains the shallow conductive layer E1 and a deeper, more discontinuous layer E2. (b) Computed rms values at each station along the profile. Stations located at the eastern and western rift shoulders show good data fit. Relatively high rms values observed for the central stations indicate an influence of 3-D features in the data which cannot be explained entirely with 2-D inversion. The outlined rectangles are segments of the 2-D section discussed in Figs 6, 7 and 8.

To analyse the contribution of individual field components, we ran inversions for all combinations of TE-, TM-mode and vertical magnetic transfer functions. In conclusion, we found that the 2-D inversion results for the upper 5 km are very robust, almost independent of the inversion settings and all data components contribute to the final inversion models. A more thorough discussion of these tests can be found in Meqbel (2009).

For the preferred 2-D inversion we used all available data components, the TE- , TM-mode and the vertical magnetic field transfer functions. To recover shallow as well as deep structures we used the full period range of the MT data from 0.001 to ∼3000 s. Static shift is an inherent problem in MT data which is caused by near surface 3-D inhomogeneities (e.g. Jiracek 1990). Since static shift acts as a frequency independent amplification, it affects only the apparent resistivity values while the phases are unaffected. To reduce the influence of static shift, a high error floor of 1000 per cent was assigned to the TE-mode apparent resistivity data, so that effectively only TE-mode phases are used for the inversion. For the TM-mode data, error floors of 5 per cent and 0.6 were set to the apparent resistivities and phases, respectively, and an error floor of 0.03 was set to the vertical magnetic components. Static shift in the TM-mode apparent resistivity data can be compensated by the inversion and is reflected by tiny near-surface heterogeneities in the model. Fig. 4(a) shows our preferred conductivity model after 2000 iterations. The rms values for individual stations in Fig. 4(b) indicate that sites located at the eastern and western rift shoulders generally show a good data fit. Relatively high rms values of the central stations indicate an influence of 3-D features, which cannot be modelled with 2-D inversion. The overall rms value computed for all stations, periods and data components is 1.81 which is acceptable for the assigned error bounds.

The model presented in Fig. 4(a) focuses on the upper 20 km of the subsurface. The most important and robust structures include the resistive blocks labelled A and B starting at depths of ∼3 km. A sequence of resistive–conductive layers extends from surface to depths of ∼3 km from the central part of the model towards the west (label C). A highly conductive structure (<4 Ωm), laterally bound between profile km 45 and 65, extends to a depth of ∼4 km (label D).

The inner part of this region exhibits resistivities <1 Ωm, located between profile km 45 and 50 and extending to a depth of ∼1.5 km. Further east, conductor D is interrupted between profile km 55 and 60 by resistive material (>50 Ωm, label D1). D1 extends laterally only a few kilometres and reaches a depth of approximately 3 km. For the eastern rift shoulder we observe conductive–resistive sequences (label E), similarly to C in the west. The uppermost conductive layer appears at a depth of ∼0.5 km (label E1) with a thickness varying between 0.1 and 0.5 km. The lowermost layer (label E2) in this sequence, which has a resistivity of ∼15 Ωm, appears at a depth of ∼2 km and seems to be discontinuous along the eastern segment of the profile. It is possible that this layer reappears at shallower depth between profile km 75 and 80 where it may be connected with conductive material of the central part of the profile (label D).

Conductor (F) in the central part of the profile is a dominating feature, which appears in all models. The conductor appears to be extending down to ∼80 km depth, reaching lowest resistivity values (<3 Ωm) at a depth of ∼50 km. Model resolution tests (Meqbel 2009) revealed that the subvertical, deep-reaching conductor F is required by the data to fit the data. Such a massive conductor would have important implications for geodynamic processes associated with the deep DST fault system. We already pointed out, however, that the area within the DSB is affected by 3-D effects. The short In-Basin profile (see Fig. 1b) was mainly measured to achieve at least some 3-D areal coverage for 3-D modelling. The MT data of the In-Basin profile are generally consistent with the data from the main profile, indicating an extension of the extremely high conductive material towards the north. However, the general geometry of the Dead Sea with its highly conductive brines and the existence of the resistive Al-Lisan salt diapir represent 3-D structures which are better explained with 3-D modelling which is beyond the scope of this paper.

In this study, we focus our discussion on structures of the upper 10 km of the 2-D conductivity model presented in Fig. 4(a). In the upper 5 km, we observe conductive layers C1, C2, E1 and E2 at the western and eastern rift shoulders and the highly conductive feature (D) in the DSB. To verify that the conductive layers C1, C2 and E1 are resolved by our data we ran several constraint inversions. For the constraint inversions, we set the resistivity values of each one of these layers to the values of the starting model (100 Ωm). During the inversion, these values were kept fixed while the rest of the model domain was free to change. This procedure was repeated for each of the layers (C1, C2, E2). Figs 5(a) and (b) show the constraint inversion results. Setting layer C1 to 100 Ωm forces the inversion to place very conductive material above and below the area of C1. The top of resistive block A appears at shallower depth close to the DSB and deepens westwards. Fixing layer E1 at the eastern rift shoulder results in a replacement of resistive with conductive material just below the fixed area. The easternmost part of conductive layer E2 appears blurred and deeper (Fig. 5b).

A comparison between the total rms values of the unconstraint inversion result (1.84, Fig. 4a) and the constraint inversion results (1.96 and 1.98 in Figs 5a and b, respectively) indicates that all three inversions can explain the data. This is not surprising considering that the imposed constraints affect only a small number of data points at a few stations. Consequently, the total rms values, which are computed for all data, hardly change. To demonstrate the impact of the constraint inversion, we need to examine apparent resistivity and phase curves at selected stations. In Fig. 5(c), we show measured (blue and red dots) and predicted data from the unconstraint inversion (solid lines) together with the results of the constraint inversions (dashed lines). Clearly, the constraint inversions result in significantly worse fits for both TE- and TM-mode data. Short-period data (<1 s) are more severely affected. The accumulation of conductive material below fixed layer C1 increases the TM-mode phases (e.g. at site 228 at periods of around 1 s) which obviously do not fit the data. Similar misfits are observed for the eastern stations for slightly longer periods between 0.1 and 1 s (e.g. site 698). In summary, the constraint inversions result in significantly increased data misfits and because longer periods are affected to phantom structures at greater depth.

4 INTERPRETATION AND DISCUSSION OF RESULTS

The 2-D inversion section in Fig. 4(a) reveals a coherent regional scale picture of the conductivity structure of the DSB and adjacent areas. The DSB and the shallow crust up to a depth of ∼3 km east and west of the DSB are dominated by conductive structures. Two blocks of high resistivity (>500 Ωm) are located underneath the western and eastern rift shoulders. The region beneath the DSB exhibits extremely high conductivity (<1 Ωm), interrupted by more resistive features (>50 Ωm) beneath the Al-Lisan Peninsula.

4.1 Geological and tectonic setting of the upper 5 km

The shallow structures to a depth of ∼5 km along the main profile (see Fig. 1b for location) are in good agreement with geological, stratigraphic and tectonic information available from the study area. Based on data from surface geology, boreholes, gravity, and magnetics, Garfunkel & Ben-Avraham (1996) published an E–W trending geological cross-section for the region just north of our profile; approximately between profile km 37 and 75 (blue line in Fig. 6b). Fig. 6(a) shows the 2-D conductivity structures together the geological cross-section of Garfunkel & Ben-Avraham (1996). The highly conductive structures coincide spatially with Quaternary to recent sediments of the Al-Lisan formation. The Al-Lisan formation which consists mainly of gravel with an intercalation of salt and clay sediments (Powell 1988; Stanislavsky & Gvirtzman 1999) seems to extend vertically to depths of ∼4–5 km in the central part (red and orange colours in Fig. 6a). The conductive basin sediments are delimited by the eastern and western boundary faults (WBF). The extremely low resistivities (<1 Ωm) observed for the top of the Al-Lisan formations suggest infiltration of hypersaline water (brines) of the Dead Sea.

The geological cross-section and the stratigraphic column of the Al-Lisan1 deep borehole (see Fig. 6b for location) indicate a salt intrusion (Al-Lisan salt diapir) underneath the Al-Lisan Peninsula. The crystalized Halite of marine origin (Garfunkel & Ben-Avraham 1996; Powell 1988) appears in the stratigraphic column of the Al-Lisan1 borehole at a depth of ∼200 m and extends to at least 3.5 km (the maximum depth of the borehole). The Al-Lisan salt diapir appears as resistive structures in our conductivity model because crystalized Halite is a rock with low porosity which acts as an insulator (e.g. Telford *et al.* 1990). Towards the western rift shoulder, the geological cross-section indicates a transition from Cretaceous and Jurassic sedimentary formations to crystalline Pre-Cambrian igneous rocks (Basement) at a depth of ∼3 km. This transition coincides with the vertical conductivity contrast in Fig. 4(a) where a sequence of alternating conductive and resistive layers (C) is juxtaposed to resistive block A. In contrast, the top of the basement of the eastern rift shoulder appears at a depth of ∼1 km in the

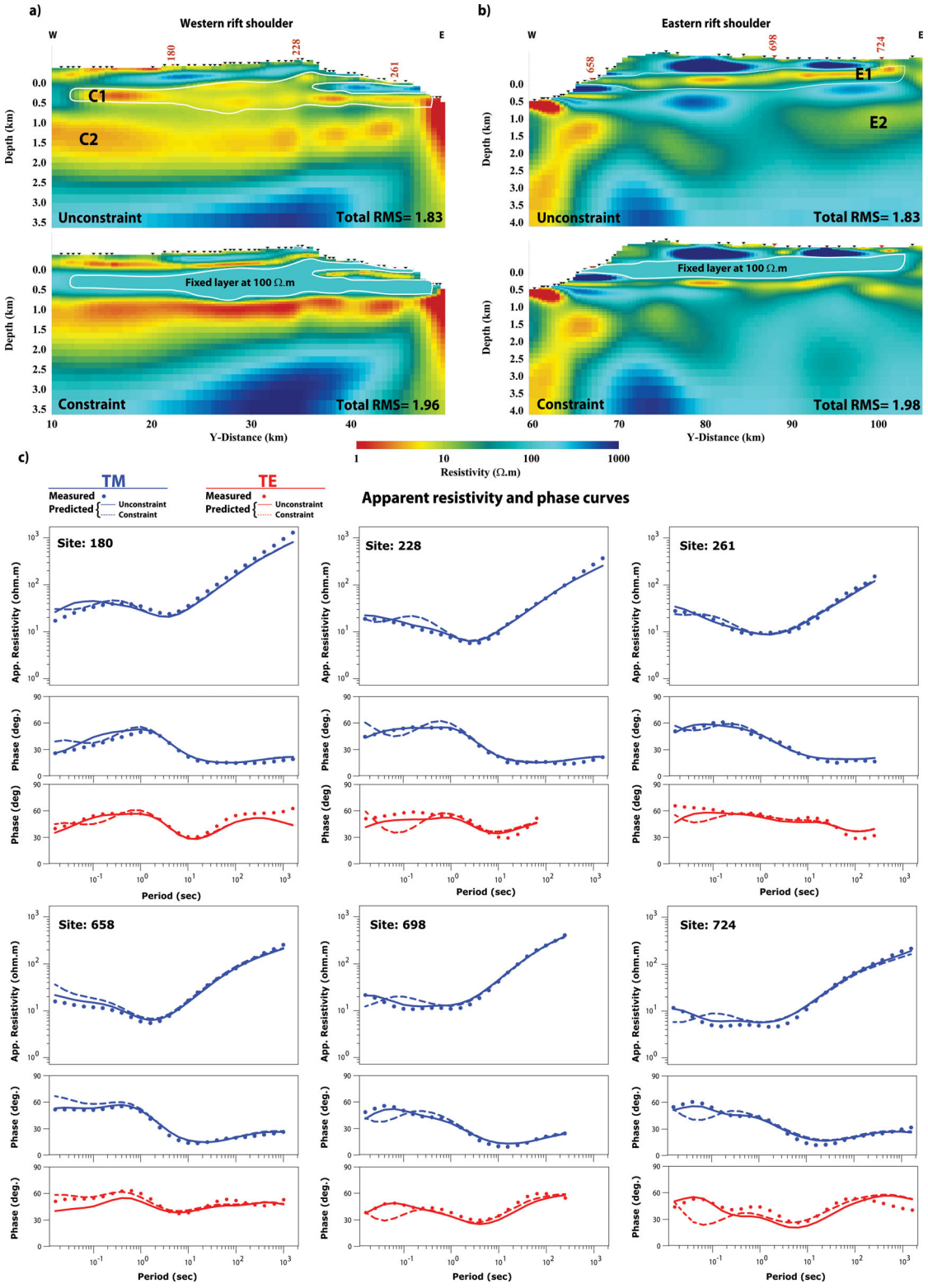

Figure 5. Model studies conducted to verify the resolution of conductive layers C1 and E1. In (a) and (b), we set the resistivity values of layers C1 and E1 to the values of the starting model (100 Ωm). During the inversion, these values were kept fixed while the rest of the model domain was free to change. A comparison between the unconstraint (upper panel) and the constraint (lower panel) inversion results shows that the inversion attempts to add additional conductive structures above and below the fixed layers to compensate for the missing conductive layers. A comparison between the total rms values of the unconstraint (1.84) and the constraint (1.96 and 1.98) inversion results indicates that fixing the conductivities of layers C1 or E1 does not affect the data fit. In (c), we plot predicted apparent resistivity and phases curves of TM (blue colour) and TE (red colour) for unconstraint (solid lines) and the constraint (dashed lines) inversions at six selected stations from the eastern and western rift shoulders. Fixing the resistivity values of layers C1 or E1 affects the data fit at periods <1 s. Interestingly, the TM data fit at sites 228 and 698 is also affected in the periods range between 0.2 and 1 s because adding additional conductive structures appears below the fixed layers.

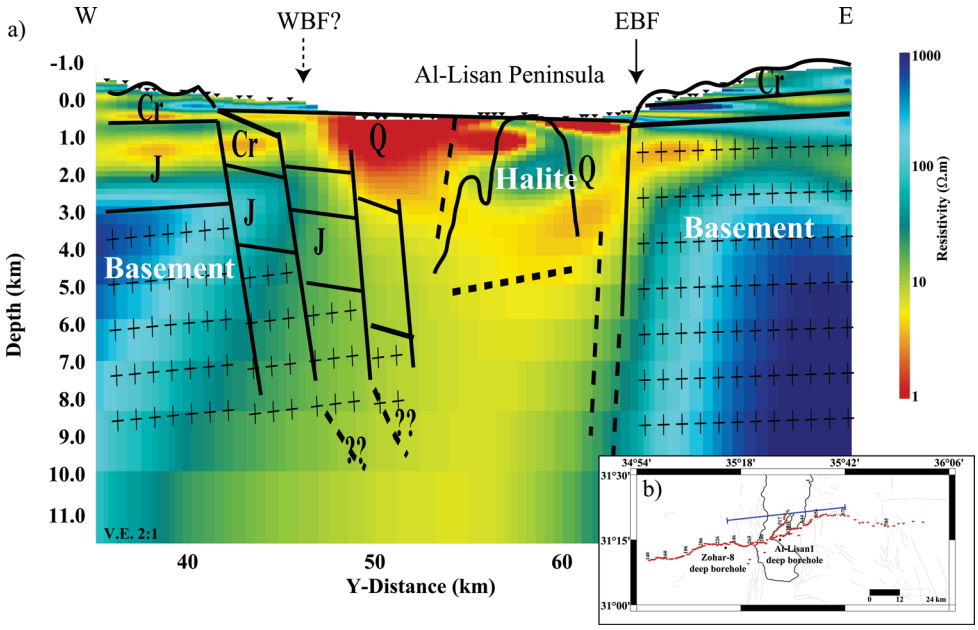

Figure 6. (a) Comparison between the central part of the preferred conductivity model (Fig. 4) and a geological cross-section (blue line in b) modified after Garfunkel & Ben-Avraham (1996). The location of the Halite intrusion defined in the geological cross-section coincides with feature D1 (in Fig. 4). The lateral transition from the western resistive block B to the central deep conductor F coincides with the trace of the Eastern Boundary Fault (EBF). However, the top of the Pre-Cambrian basement does not coincide with the top of block B. The location and depth extend of Quaternary formation (Q) coincides with conductor D. At the western side, the interface between the Cretaceous (Cr) and the Jurassic (J) is located at the bottom of the shallow conductive layer C1. Deep conductive layer C2 is embedded in thick Jurassic formations. The interface between the upper crustal sedimentary formations (Cretaceous and Jurassic) and the crystalline Pre-Cambrian igneous rocks coincides with the top of resistive block A in the West. (b) indicates the location of the geological cross-section (blue line) together with the A-Lisan peninsula and the Zohar-8 deep borehole (black dotes).

geological cross-section which does not match the top of resistive block B, imaged at a depth of ~2.5 km. The 2-D *P*-wave velocity model obtained from the DESIRE WRR (Wide-Angle Refraction Reflection) data shows the top of the seismic basement (*P*-wave velocities greater than 5.6 km s^{-1}) at a depth of approximately 2 km in the vicinity of the DSB, deepening outwards to reach approximately 6 km at the eastern and western ends of the seismic profile (Mechie *et al.* 2009).

The surface trace of the left-lateral eastern boundary strike-slip fault (EBF) appears to coincide with a sharp lateral transition from conductive structures underneath the central part of the profile to the resistive block B at a depth of ~2 km. The WBF, on the other hand, consists of several normal faults (Garfunkel 1981; Garfunkel *et al.* 1981). These normal faults dip eastwards (into the rift) and form a step-like formation (Fig. 6a). The rocks at the western margin of the DSB are therefore strongly fractured and deformed assemblages of igneous Pre-Cambrian rocks mixed with the overlying sedimentary formations of the Jurassic and Cretaceous. The MT model reveals only a volume integrated conductivity of this structure.

Further to the west, we can correlate the conductivity model with the stratigraphic column of the Zohar-8 deep borehole (see Fig. 6b for location; Gilboa *et al.* 1993), which reached a depth of more than 2.5 km. Fig. 7(a) shows a comparison between the conductivity model and stratigraphic column of the Zohar-8 borehole, which covers formations from the Cretaceous to the Pre-Cambrian. Two vertical discontinuities of our conductivity model appear to correlate with lithological changes. The first is the transition from the Cretaceous to the Jurassic sequences which coincides with the lower boundary of conductive layer C1. The second discontinuity is the transition from Cretaceous, Jurassic, Triassic and Permian sedimentary formations to basement rocks which coincides with the transition from resistive–conductive sequences C to the resistive western block A (see Fig. 4). Closer inspection of the stratigraphic column of the Zohar-8 borehole reveals further details. For instance, the upper and lower Cretaceous (Judea and Kurnub groups, respectively) are imaged as two conductive horizons separated by a resistive layer. The Judea (predominantly platform carbonates) and the Kurnub (Sandstone) formations are the two main regional aquifers at the western rift shoulder (Stanislavsky & Gvirtzman 1999; Gvirtzman & Stanislavsky 2000; Kafri & Goldman 2005). It is interesting to note that the two separate conductive layers, which coincide with the Judea and Kurnub groups, seem to merge and continue westwards as a single conductive layer. The upper Jurassic (top of Arad group) shows higher resistivity values than the lower Jurassic. Transitions from the lower Jurassic to the Triassic (Ramon group) and from the Triassic to the Permian are not revealed in the conductivity model. Several normal faults have been mapped in the vicinity of the Zohar-8 borehole (labelled F1, F2, F3 in Fig. 7a). Interestingly, these faults appear to partition conductors C1 and C2 laterally into blocks of high conductivity.

As there are no deep boreholes on the eastern rift shoulder, the stratigraphic information is assembled from surface geology and hydrogeological information and by comparison with the western rift shoulder (Fig. 7b). From surface geology, Khalil (1992) and Powell & Basem (2011) identified the upper and lower Cretaceous as the Ajloun (mainly limestone) and the Kurnub (sandstone) groups, respectively. Taking into account the differences in uplift rates between the western and eastern rift shoulders (Garfunkel *et al.* 1981), it seems plausible that the shallow conductive layer E1 coincides with the Kurnub Sandstone group. This hypothesis is supported by the depth to the top of E1 which seems to be shifted upwards by ~500 m relative to the top of C1 (Kurnub group; Fig. 7a). In the

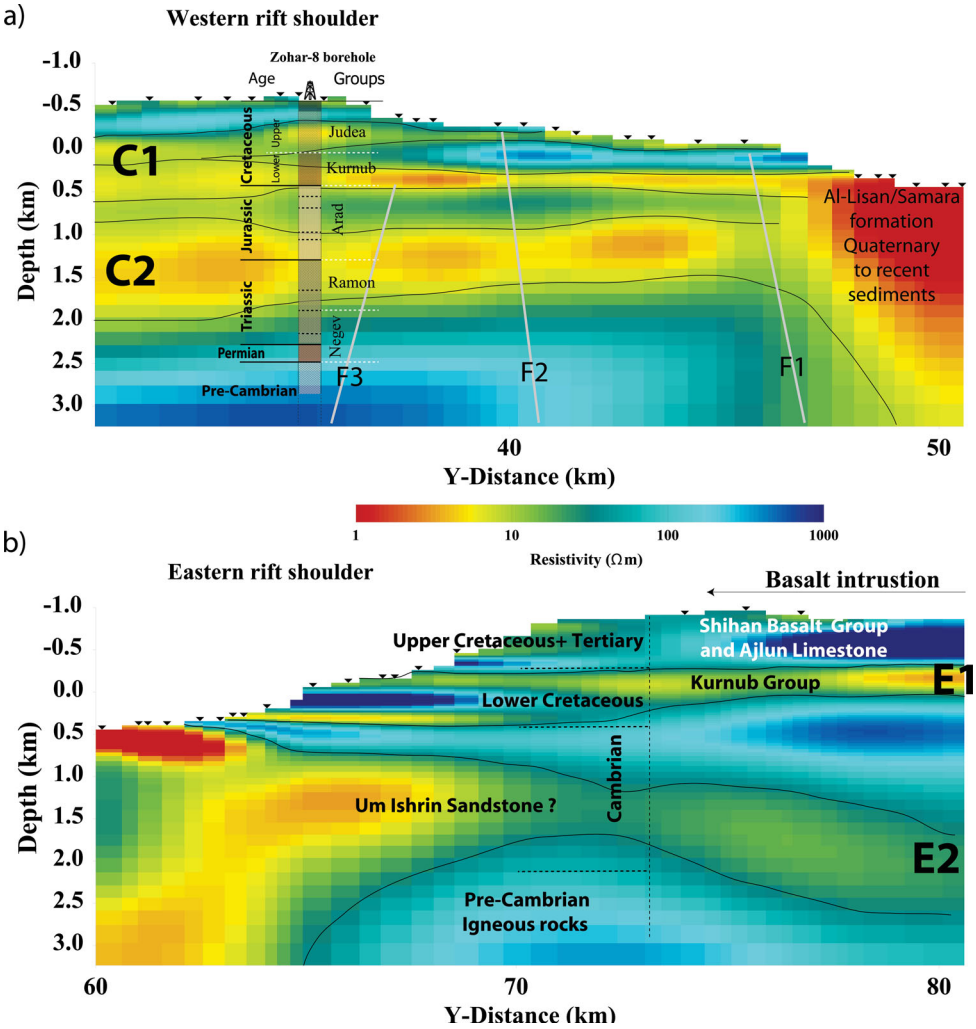

Figure 7. Geological information superimposed on the 2-D conductivity section: (a) For the western rift shoulder, we use the stratigraphic column of the Zohar-8 borehole to constrain the interpretation of the conductivity model. The transition from the Cretaceous to the Jurassic is coincides with the base of layer C1 (Kurnub group). The upper and lower Cretaceous (Judea and Kurnub groups) are imaged as two conductive horizons separated by a more resistive layer which thickens eastwards. The base of the Arad group and the top of the Ramon group are integrated into conductive layer C2. Solid lines labelled F1, F2 and F3 indicate approximate positions of three major normal faults inferred from the geological cross-section of Stanislavsky & Gvirtzman (1999). (b) Major geological units at the eastern rift shoulder, assembled from geological and hydrogeological information. It seems plausible to interpret conductive layer E1 as the Sandstone of Kurnub group. Due to a differences in the uplift rate between the eastern and western rift shoulders, the top of the Kurnub group is higher (from sea level) than at the western rift shoulder. Comparison with surface geology suggests that highly resistive regions in the conductivity model correlate with the Shihan Basalt intrusion. Based on hydrogeological information, we speculate that the conductive layer E2 could coincide with Um Ishrin Sandstone of the Cambrian which is known to contain brines (Khalil 1992).

Neogene–Quaternary (6 Ma), the Jabal Shihan volcano erupted and basaltic lava covered a broad area of the eastern rift shoulder (Masri 2003). The basaltic formations appear as highly resistive structures from surface (~900 m above sea level) to depths of ~300 m (which results in a total thickness of ~600 m). The Jurassic is missing in the stratigraphic column of the study area at the eastern rift shoulder (Khalil 1992). The Triassic–Permian strata consist mainly of sandstones in alternation with siltstones (Umm Irna sandstone). The relatively thin Umm Irna sandstones (max. 80 m) are underlain by the Cambrian Umm Ishrin sandstone which varies in thickness from 300 to 330 m. The deeper conductive layer E2 may be linked with the Cambrian Um Ishrin sandstone which was identified as a deep aquifer (brines) by (Khalil 1992, and references herein). We interpret the top of the resistive block B at a depth of ~3 km as basement (Pre-Cambrian).

4.2 Hydrogeological system

The main aquifers in the study area are upper Cretaceous limestones (Ajloun/Judea), lower Cretaceous sandstones (Kurnub) and the alluvial Quaternary Dead Sea formations (Al-Lisan/Samara; Stanislavsky & Gvirtzman 1999; Gvirtzman & Stanislavsky 2000; Salameh & El-Naser 2000; Ben-Itzhak & Gvirtzman 2005; Kafri & Goldman 2005; Eraifej 2006; Yechieli 2006; Salameh & Hammouri 2008). In addition, Khalil (1992), Fleischer *et al.* (1977) and Stanislavsky & Gvirtzman (1999) reported on the existence of deep brines beneath the eastern and western rift shoulders in the Cambrian and the Jurassic/Triassic formations. Comparison with the conductivity model in Fig. 8 indicates that aquifers and occurrences of deep brines could coincide with the conductive layers observed at both sides of the rift valley. East of the Zohar-8 borehole (Fig. 8a), the

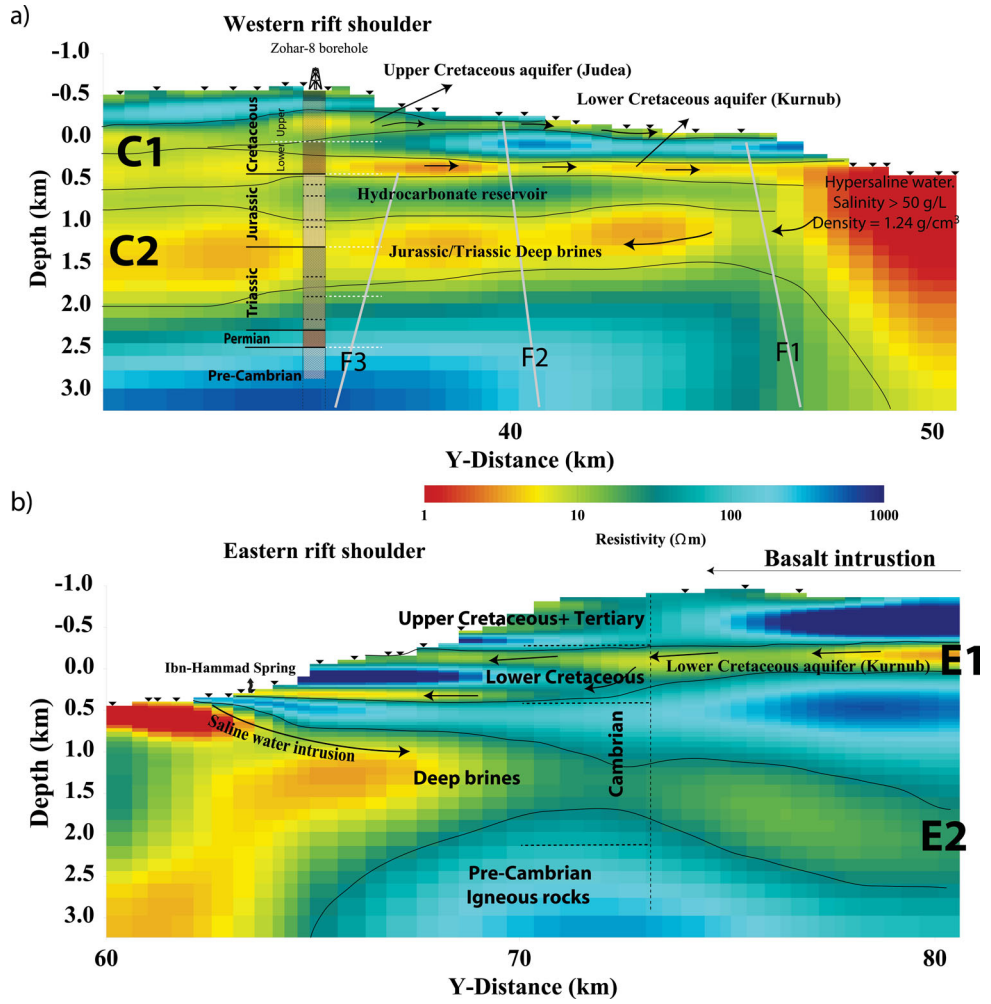

Figure 8. The conductivity model superimposed with major hydrogeological units (aquifers): (a) At the western rift shoulders, the Judea and the Kurnub groups are the two major aquifers of the upper and lower Cretaceous. Based on chemical analysis of groundwater from deep boreholes in the study area (Fleischer *et al.* 1977) and the hydrodynamic model of Stanislavsky & Gvirtzman (1999), we interpret the high conductivity associated with the Jurassic and Triassic as deep brines. In the Dead Sea Basin, the Al-Lisan/Samara formation host the so-called Dead Sea aquifer. The extremely high conductivity observed in and beneath the Dead Sea Basin implies that the Al-Lisan/Samara formation is highly porous and that hypersaline water of the Dead Sea brines can penetrate to several kilometres depth. (b) Towards the eastern rift shoulder, the lower Cretaceous Kurnub aquifer seems to become shallow towards the eastern end of the model and to deepen westwards near the Dead Sea. Following the arguments for the western rift shoulder (see text), we speculate that the Dead Sea brines flow eastwards in the deep aquifer of Um Ishrin due to density-driven forces (see text). This could also explain the very low resistivity observed in direct vicinity of the Dead Sea. Interestingly, for the western rift shoulder we observe a concentration of conductive structures between the system of normal faults (grey lines in a). This could imply that these faults are semi-permeable preventing a free flow of the groundwater: eastwards in Kurnub aquifer and westwards into Jurassic/Triassic layers.

two main aquifers at the western rift shoulder (Judea and Kurnub) are imaged as two separate conductive layers. West of the borehole the two separated conductive layers appear to merge and continue as conductive layer C1 in the MT image. However, distinguishing the two aquifers along the entire profile may be beyond the resolution of the method.

Based on hydrodynamic modelling, Stanislavsky & Gvirtzman (1999) and later Gvirtzman & Stanislavsky (2000) concluded that two main forces control the water flow in the vicinity of the Dead Sea rift (see arrows in Fig. 8). Topography-driven ground water flow in the shallow aquifers (Judea and Kurnub) is towards the rift valley. The second force is density-driven. The relatively higher density of Dead Sea brines (1.24 g cm^{-3}), when compared with meteoric water, effectively result in an east- and westward directed flow away from the rift valley. Moreover, Gvirtzman & Stanislavsky (2000) concluded that density-driven forces could be responsible for hydrocarbon migration from source rocks in the rift valley to the top of the Jurassic (Arad group) at the western rift shoulder.

Fig. 9 shows a compilation of the main geological and hydrological features based on the interpretation of the conductivity model obtained along the main profile. The upper 3–4 km of the model indicate sedimentary formations at the eastern and western rift shoulders which accommodate the shallow Judea and Kurnub aquifers as well as the deep brines of the lower Jurassic and upper Triassic. These sedimentary formations are underlain by crystallized igneous rocks of the Pre-Cambrian (basement). Due to the smoothing effect of the 2-D inversion algorithm, it is difficult to determine an exact depth to the top of the basement. Assuming minimum values of 300 Ωm for the top of the basement (dark blue colours), the western rift shoulder seems to deepen westwards, in agreement with borehole information (Gvirtzman 2004).The very conductive sedimentary formations beneath the DSB extend

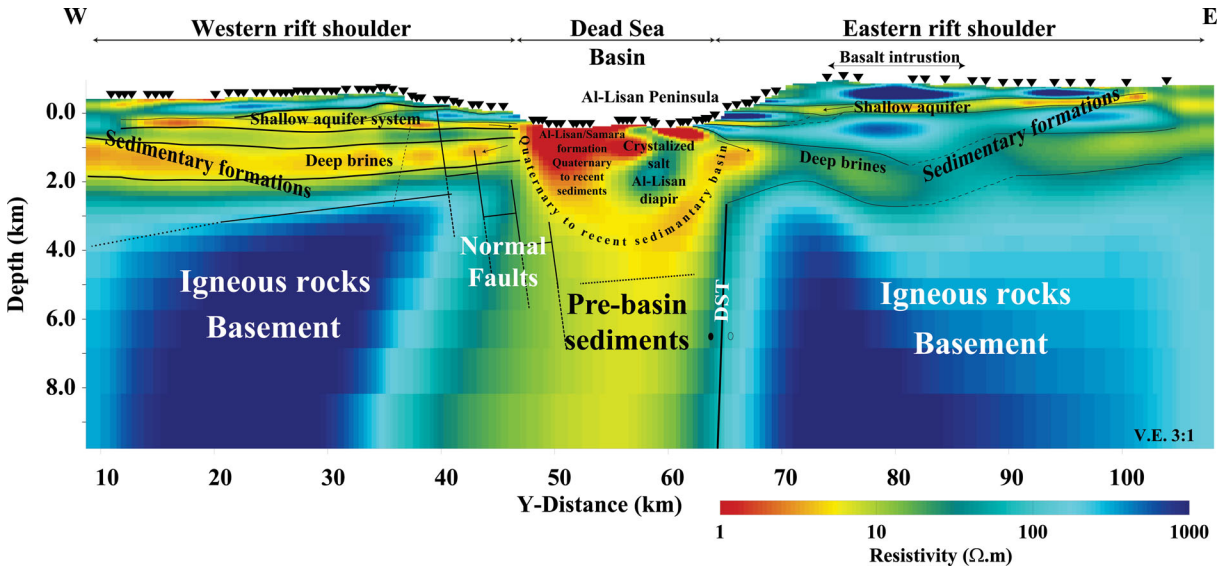

Figure 9. Geological and hydrological interpretation superimposed on the 2-D conductivity model. The sedimentary formations of the Cretaceous to the Triassic dominate the model to a depth of ∼3 km on both sides of the rift valley. The sedimentary formations at the eastern and western rift shoulders are underlined by massive crystallized igneous rocks of the Pre-Cambrian (basement). We observe for the western rift shoulder that the top of the basement becomes shallower close to the Dead Sea Basin and deepens westwards. The basement underneath the Dead Sea Basin is separated by more conductive structures which may relate to Pre-Basin sediment that have accumulated in a deeply fractured zone. The brine-saturated sedimentary formations of Dead Sea Basin extend vertically down to a depth of ∼5 km. The highest conductivities (salinities) are observed at depths of up to ∼2 km. The crystallized rock salt of the Al-Lisan diapir is located directly underneath the Al-Lisan Peninsula reaching a depth of ∼3 km. Also shown are the strands of the Dead Sea transform fault (DST) which delimit the Dead Sea Basin horizontally and normal fault systems at the eastern and western margins, respectively.

vertically to depths of up to 5 km (red and orange colours). The high conductivity can be explained with highly saline pore fluids; the highest salinities are observed in the upper ∼2 km. The sedimentary formations of DSB are underlain by older (Pre-Basin; Garfunkel & Ben-Avraham 1996) sediments which could be deeply fractured due to shearing processes associated with the DST fault system. We interpret the sharper, subvertical transition from conductive to resistive material at the eastern rift shoulder as an expression of the left-lateral strike-slip DST fault, while the western shoulder appears to be dominated by a wider system of normal faults. The highly conductive and possibly brine-saturated sedimentary formations of the DSB are interrupted by the crystallized (therefore resistive) rock salt of the Al-Lisan salt diapir underneath the Al-Lisan Peninsula.

As mentioned before, we interpret the very low resistivities directly underneath the DSB as highly porous sedimentary sequences of the Al-Lisan/Samara saturated with hypersaline water of the Dead Sea brines. To quantify this statement and to estimate a maximum penetration depth of the Dead Sea brines, we use the simplest form of Archie's empirical law (Archie 1942)

$$\rho_b = \rho_f \Phi^{-m}. \quad (1)$$

Eq. (1) relates the bulk resistivity ρ_b of sedimentary rocks to the formation water resistivity ρ_f, porosity Φ and cementation factor m. Archie's law implies that in highly porous rocks with low cementation factor, the bulk resistivity is dominated by the formation water resistivity. The problem in applying Archie's law is that we measure only the bulk resistivity with MT. Hence, estimating the other three unknown parameters requires *a priori* information. According to Kafri & Goldman (2005), the cementation factor m varies between 1.8 and 2 for consolidated sand. Since the Al-Lisan/Samara formations contain clay which could increase the cementation factor, we chose an upper limit of 2 for m. Kafri & Goldman (2005) argued that the other unknowns in Archie's law can be accurately estimated in areas where saline water intrusion can be expected because the salinity and electrical resistivity of the intruded sea water is known. Kafri & Goldman (2005) used a value of 0.04 Ωm for saline water (ρ_f) of the Dead Sea brines. Based on TDEM measurements carried out at the western flank of the DSB, Kafri & Goldman (2005) and Levi *et al.* (2008) suggested that rock formations with bulk resistivity values <1.0 Ωm are saturated with hypersaline fluids. Using these information ($\rho_f = 0.04$ Ωm, $m = 2$) and the resistivity values from the 2-D inversion models, we can calculate the salinity distribution of the shallow crust underneath the DSB. We used the relationship $6400 \times \sigma_f$ to convert fluid conductivities into salinities (TDS) measured in mg l^{-1} (Rhoades *et al.* 1999).

Fig. 10(a) shows regions where the 2-D model yields bulk resistivity values ≤ 1 Ωm in the DSB. These highly conductive structures extend to a depth of ∼1.5 km and are delimited by the Al-Lisan salt diapir in the east. To estimate the porosity of the Dead Sea coastal aquifer, we use Archie's law, assuming $\rho_f = 0.04$ Ωm and $m = 2$. Fig. 10(b) shows the resulting porosity distribution for values >0.1 (10 per cent), with an average value of 0.24. Fig. 10(b) shows that the porosity decreases gradually both in horizontal and vertical directions away from the central part at shallow depth. This reflects the resistivity variations of the 2-D inversion section which is to some extent influenced by a smoothing effect (regularization). On the other hand, it can be expected that porosity decreases with depth as a consequence of the sedimentation process. It is unclear, however, why porosity should change rapidly in the horizontal direction over a short distance. To avoid the influence of smoothing we can estimate a most common value of the bulk resistivity. Fig. 10(c) shows a bar chart of occurrences of ρ_b. The inversion section reveals resistivity values in the range $0.06 < \rho_b < 1.0$ Ωm. A value of 0.3 Ωm is the most common value in the considered range (yellow shaded area).

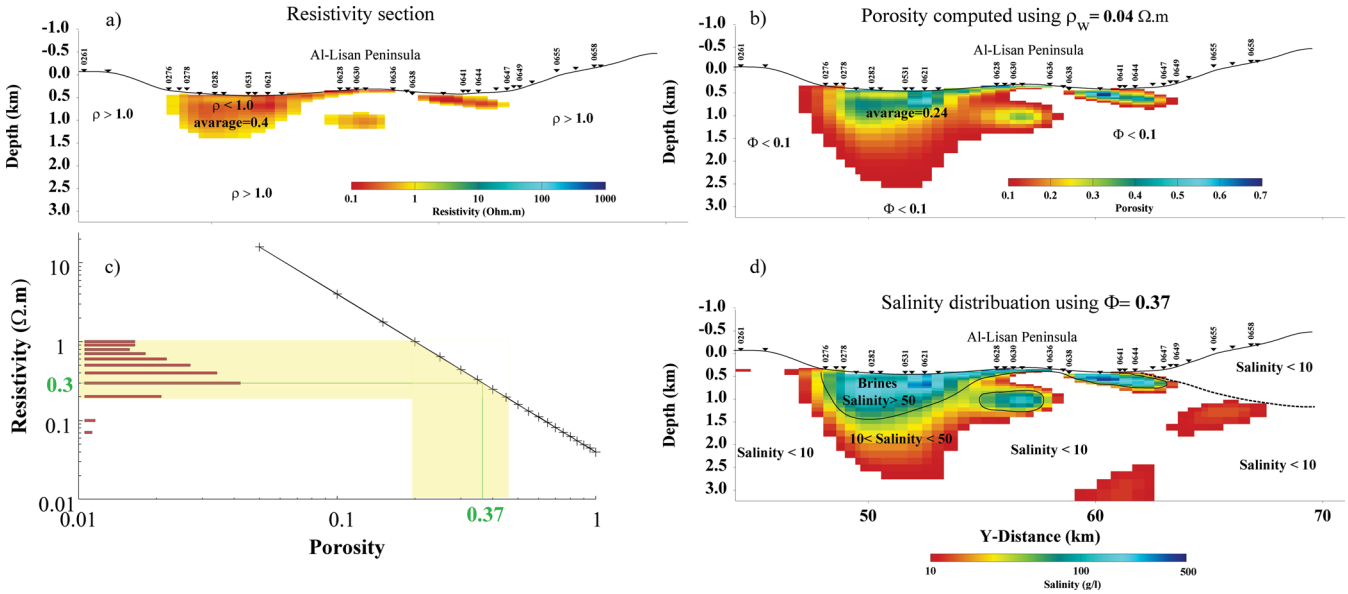

Figure 10. (a) Areas which exhibit resistivity <1.0 Ωm in the Dead Sea aquifer which is hosted in the Al-Lisan/Samara formation. (b) Assuming that the aquifer is saturated with hypersaline brines of the Dead Sea (0.04 Ωm), we can deduce a porosity distribution. Assuming 10 per cent as a lower limit for porosity, (b) reveals that high porosity between 30 and 40 per cent is limited to the upper 1 km of the section. Porosity (ϕ) values between 0.1 and 0.2 dominate deeper structures. To a depth of ∼2.5 km, we observe resistivites <2.0 Ωm. (c) Distribution of bulk resistivity values in the range between 0.06 and 1 Ωm (yellow shaded area). The most frequently observed resistivity value of 0.3 Ωm, corresponding to more than 30 per cent of the resistivity values, requires a porosity of 0.37 (green line) when we assume a formation water resistivity of 0.04 Ωm. The black line in (c) shows this relation between bulk resistivity and porosity. (d) When assuming a value of 0.37 for the porosity of the Al-Lisan/Samara formation, we observe salinity values >50 g^{-1} (brines) for the upper 1.5 km. and salinities between 10 and 50 g^{-1} for depths of up to ∼2.5 km. The dashed line underneath the eastern rift shoulder represents an interface below which the salinity is less than 10 g^{-1}.

The black line in Fig. 10(c) indicates the relation between bulk resistivity and porosity ranging from 1 to 0.05 for a fixed value of ρ_f (0.04 Ωm). The most frequently observed (average) resistivity of 0.3 Ωm corresponds to a porosity of 0.37. Such a porosity is in agreement with the observation by Kafri & Goldman (2005) who estimated a range between 0.2 and 0.4 for the Al-Lisan/Samara formations. Alternatively, we can fix the porosity to estimate salinities from the 2-D resistivity section. Fig. 10(d) shows the salinity distribution for the Al-Lisan/Samara formations if we assume an average porosity of 0.37. Salinities are in a range between 10 and 500 g l^{-1} and the highest salinities (>10 g l^{-1}) are found mainly west of the Al-Lisan Peninsula. A small region of high salinity appears also east of the Al-Lisan salt diapir.

Assuming a porosity of 0.37 for the entire Dead Sea costal aquifer, Fig. 10(d) would indicate water with salinity >50 g l^{-1} (brines) to occur to depths of up to 1.7 km and with salinities between 10 and 50 g l^{-1} to depths of approximately 2.7 km. Such a distribution of salinities at greater depths would imply brackish pore fluids (salinities between 10 and 50 g l^{-1}; Fleischer *et al.* 1977) for the bottom of the Dead Sea costal aquifer, overlain by (saturated) brines. Effectively, this would result in a hydrological reversal which contradicts hydrological conditions. A more plausible interpretation for the observed low resistivity values at depths >∼2 km) would be reduced porosity due to increased lithostatic pressure, possibly accompanied with to crystallization of salt minerals which can have a sealing effect. The porosity distribution map in Fig. 10(b) indicates decreasing porosities (between 0.1 and 0.2) for a depth range between 1.5 and 2.7 km. Remarkable in Figs 8(b) and 10(d) are the very low resistivity and therefore high salinity values, observed close to the eastern shore of the Dead Sea. Due to the high salinity and density of the Dead Sea brines, Salameh & El-Naser (2000); Kafri *et al.* (1997) suggested that the saline/fresh water interface is nine times shallower close to the Dead Sea than for normal sea water conditions. Using the computed salinity value distribution at the eastern shore line of the Dead Sea, we infer an interface below which the formations can be expected to be saturated with hypersaline to brackish water (dashed line in Fig. 10 d). Near the western shore of the Dead Sea, we could not install MT stations because of the steep topography. Hence, we cannot resolve possible interfaces between saline, brackish, and fresh water.

Figs 8(a) and (b) reveal an inhomogeneous conductivity distribution of the Judea and Kurnub aquifers. The bulk resistivities vary between 3 and 20 Ωm (bars in Fig. 11a). According to Archie's law, variations in bulk resistivity imply variations either in porosity or fluid resistivity (ρ_f). In a hydrodynamic study carried out to simulate the migration of continental-rift brines, Stanislavsky & Gvirtzman (1999) and later Gvirtzman & Stanislavsky (2000) used a porosity of 0.15 and 0.05 for the upper and lower Judea group, respectively, and a value of 0.1 for Kurnub group. Shalev *et al.* (2007), on the other hand, suggested porosity values of 0.1 for both the Judea and Kurnub groups in their heat flow simulation study. Based on TDEM measurements, Kafri & Goldman (2005) found porosity values between 0.15 and 0.20 as representative for the Judea group carbonates, assuming saturation with normal sea water (0.18 Ωm). Following this idea, we postulate sea water saturation for the Judea and Kurnub aquifers and computed corresponding bulk resistivity values. The yellow shaded area in Fig. 11(a) shows variations of bulk resistivity values observed for the Judea and Kurnub groups (bars) plotted versus porosity. The black line in Fig. 11(a) is computed using eq. (1) and for porosity values ranging between 1 and 0.01. The minimum, maximum and average porosity values, corresponding to respective maximum, minimum and average bulk

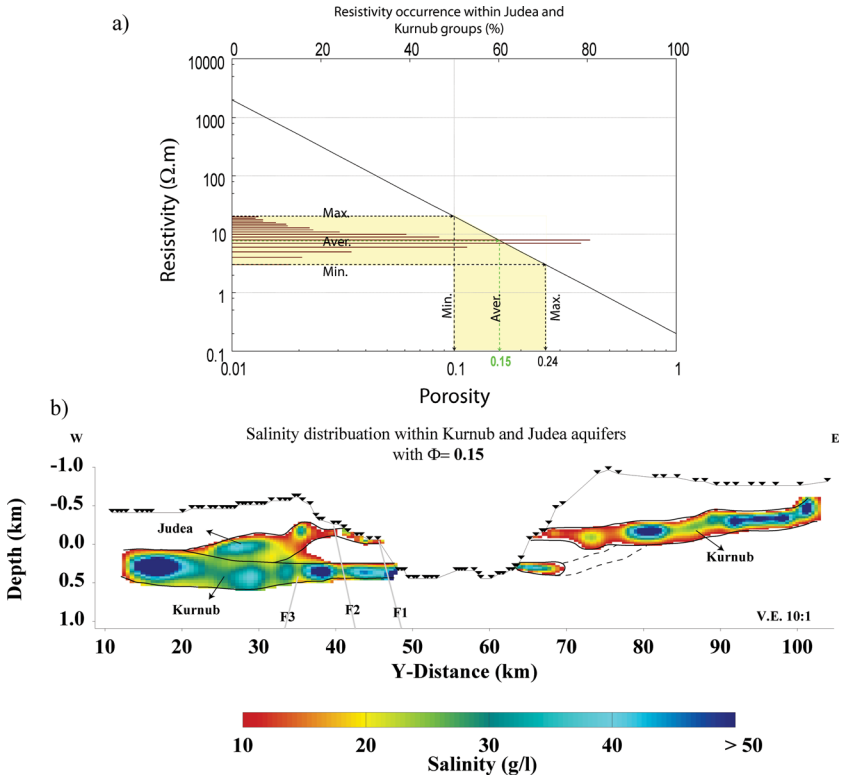

Figure 11. Porosity and salinity distribution of the Judea and Kurnub aquifer calculated using Archie's law and the upper part of the 2-D resistivity section shown in Fig. 4 (see text).

resistivity values, are 0.1, 0.24 and 0.15. Considering that more than 20 per cent of the bulk resistivity values are between 5 and 11 Ωm, we conclude that the Judea and Kurnub groups have an average porosity of 0.15 (the average porosity which corresponds to the average bulk resistivity of 8.4 Ωm).

Since the Kurnub aquifer is hosted in the same stratigraphic unit (Kurnub group of the lower Cretaceous) on the eastern and western rift shoulders, it seems also plausible to use the same porosity values for both sides of the rift. Using a porosity value of 0.15 and the observed bulk resistivity values we computed the salinity distribution of the Judea and the Kurnub aquifers on both sides of the rift (Fig. 11b). The computed salinity varies between 10 and >50 g l^{-1}. In general, the Kurnub aquifer at the western rift shoulder shows higher salinity than the overlying Judea aquifer and the Kurnub aquifer at the eastern rift shoulder. The high salinity of the Kurnub aquifer near the Dead Sea in the west is remarkable; it could imply an intrusion of Dead Sea brines. Close to the discharge areas of the Judea and the eastern Kurnub aquifers at the western and eastern escarpments of the Dead Sea, we observe relatively low salinity values (∼10 g l^{-1}). At the discharge area of the lower part of the eastern Kurnub aquifer near the Dead Sea, however, the salinity reaches value of ∼30 g l^{-1}. This is in good agreement with chemical analyses of ground water and springs along the eastern escarpment of the Dead Sea which indicates salinity reaching ∼40 g l^{-1} near our study area (in Gohr Hadetha; Salameh & Hammouri 2008). The water from the three largest springs along the western escarpment of the Dead Sea (Tsukim, Kane and Samar) originates from the Judea group aquifer (Ben-Itzhak & Gvirtzman 2005). Water salinity of the Tsukim spring, for instance, which is located a few kilometres north of our study area ranges between 1.7 and over 40 g l^{-1}. It is interesting to note that the highest salinity values (>50 g l^{-1}) were found for the western Kurnub aquifer group, concentrated in areas between faults (grey lines in Fig. 11).

Porosity and salinity of the lowest conductive layer (deep brines of the Jurassic/Triassic; C2 in Fig. 4) is estimated using the same procedures. The bulk resistivity of the deep Jurassic/Triassic brines ranges between 4 and 20 Ωm with an average value of ∼6 Ωm. Stanislavsky & Gvirtzman (1999) and later Gvirtzman & Stanislavsky (2000) concluded that for the last 3–6 Ma Dead Sea brines migrated westwards in deep aquifers driven by their relatively higher density. Thus, it seems plausible that the deep Jurassic/Triassic aquifer is at least partly saturated by Dead Sea brines. Similar to the diagrams in Figs 10(c) and 11(a), we computed bulk resistivity values using Archie's law for porosity values between 0.01 and 1 and assuming 0.04 Ωm for ρ_f. Fig. 12(a) shows that a porosity of ∼0.07 is required to explain the observed average bulk resistivity of ∼6 Ωm. A porosity of 0.07 for the Jurassic/Triassic is in good agreement with a value of 0.05 used for hydrodynamic and heat flow simulation by Stanislavsky & Gvirtzman (1999) and Shalev *et al.* (2007), respectively. For Fig. 12(b), we used a porosity of 0.07 and a range of bulk resistivity values (between 4 and 19 Ωm) to estimate salinities for the Jurassic/Triassic groups, which range between 70 and ∼300 g l^{-1}. Similarly to the overlying Kurnub aquifer, the highest salinities of the Jurassic/Triassic groups are observed between faults. Faults can act as semi-permeable barriers of fluid flow (e.g. Ritter *et al.* 2003) and low bulk resistivity and high salinity could be due to an accumulation of saline water between faults.

5 CONCLUSION

A continuous MT transect crossing the entire DSB, from the eastern to the western rift shoulders and beyond reveals a comprehensive

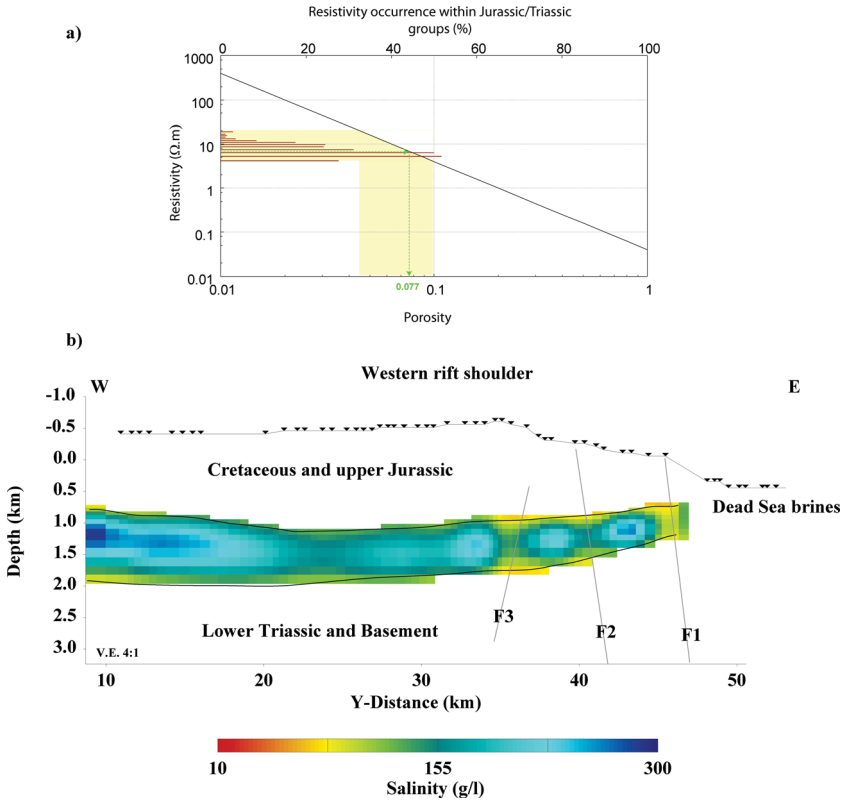

Figure 12. Porosity and salinity distribution of the Jurassic/Triassic deep brines calculated using Archie's law and the upper part of the 2-D resistivity section shown in Fig. 4 (see text).

picture of the subsurface electrical conductivity structures from the basin and adjacent areas. The 2-D inverse model provides insights into the geological and hydrological system of the DSB and adjacent areas. The overall picture of the DSB and its vicinity comprises a series of conductive and resistive layers observed at the eastern and western rift shoulders up to a depth of ∼3 km. Extremely high conductivities (≤ 1 Ωm) are observed within the DSB up to a depth of ∼1.5 km, followed by moderate conductivity structures up to a depth of ∼4 km. Two blocks of high resistivity (>500 Ωm) are located underneath the western and eastern rift shoulders. The most palpable conductivity contrast in our 2-D model is an abrupt lateral transition from the resistivity block underneath the eastern rift shoulder to the conductive structures within the DSB.

Quaternary to recent sediments of the Al-Lisan/Samara formations are expressed as highly conductive structures reaching a depth of approximately 4 km. East and west of the rift valley layered sequences of resistive and conductive structures coincide with the sedimentary formations of the Cretaceous, Jurassic and Triassic. Pre-Cambrian basement (crystalized igneous rocks) appears at depths >3 km beneath both rift shoulders as very resistive regions. The EBF of the DST is associated with a sharp lateral conductivity contrast between the highly resistive basement structures and the conductive fill of the DSB. The transition to the western rift shoulder appears wider and smoother, in agreement with a wider fractured region, possibly caused by a combination of strong normal faulting and strike-slip activity.

From the electrical conductivity images and estimating porosities of the sedimentary rocks, we can infer salinities for the various aquifers. Variations of conductivity observed within the sedimentary formations at the eastern and western rift shoulders imply changes in the groundwater content and composition (degree of salinity). The regional Judea and Kurnub aquifers of the Cretaceous are imaged as conductive layers with resistivities of 1–20 Ωm, for which we infer porosities of 15 per cent. The low resistivities observed in the Jurassic/Triassic formations can be explained with highly saline or saturated brines and a porosity of 7 per cent. Assuming that the Dead Sea costal aquifer is saturated with Dead Sea brines, a porosity of 37 per cent is required to explain the extremely high conductivities. For the Al-Lisan/Samara formations, salinities reach values >50 g l^{-1} in the upper 1.7 km. The Judea, Kurnub and Jurassic/Triassic aquifers have a more inhomogeneous distribution of salinity with highest values observed between normal faults at the western rift shoulder. Salinity values derived from the fluid resistivities of the regional aquifers at the eastern and western rift shoulders imply generally increasing salinity with depth.

The very high conductivities of less than 1 Ωm of the Al-Lisan/Samara formations can be explained with hypersaline waters of the Dead Sea reaching depths of a few kilometres and porosities of at least 37 per cent. The highest salinities reaching values of approximately 200 TDS are observed in the upper 1.7 km of the Dead Sea costal aquifer.

The porosity and salinity sections for conductive structures inside and in the vicinity of the DSB (Figs 10, 11 and 12) are based on constraints from existing geoelectrical studies, hydrodynamic modelling, heat flow simulations and chemical analysis of ground water from boreholes and springs. Computation of porosities and salinities requires further assumptions, including a simplified version of Archie's law. Nevertheless, our derived porosities are generally in a good agreement with published data. Clearly though, our results are indirect measures of porosity (and salinity) and these results should be taken with care. However, in any case, the sequence of conductive and resistive horizons found on the western and eastern

side of the DSB and their interpretation are important to understand the hydrological system of this region

ACKNOWLEDGEMENTS

We thank the National Ministry of Infrastructure of Israel, the Natural Resources Authority of Jordan and the An-Najah University in Nablus, the Palestine Territories for their support throughout this project. We thank the military, security and customs agencies of Israel and Jordan for their help. The MT instruments were provided by the Geophysical Instrument Pool of the GeoForschungsZentrum Potsdam. The DESIRE project was funded by the Deutsche Forschungsgemeinschaft and the GeoForschungsZentrum Potsdam. We gratefully thank Dr Weckmann, Dr Munoz and Dr Becken for their enthusiastic help in the field and overall in processing and discussing the DESIRE-MT data. We would like to extend our heartfelt thanks to all people who helped collecting DESIRE-MT data in Jordan and Israel: Jana Börner, Romina Gehrmann, Olaf Helwig, Juliane Hübert, Thomas Krings, Christian Mielke, Stefanie Musiol, Stefan Rettig, Manfred Schüler and Wenke Wilhelms (Germany). Khalil Abu-Ayyash, Khaldon Abu Hamideh, Darwish Jaser, Jamal Khataibeh, Issam Qabbani, Husam Al-Rashdan and Tahsin Tal'at (Jordan). Yossi Bartov, Uri Frieslander and Gabby Heim (Israel). The authors would like to thank the anonymous reviewers for their valuable comments and suggestions to improve the quality of the paper.

REFERENCES

Archie, G.E., 1942. The electrical resistivity log as an aid in determining some reservoir characteristics, *Trans. Am. Inst. Min. Metall. Pet. Eng.,* **146,** 54–62.

Bahr, K., 1988. Interpretation of the magnetotelluric impedance tensor: regional induction and local distortion, *J. Geophys.,* **62,** 119–127.

Becken, M. & Burkhardt, H., 2004. An ellipticity criterion in magnetotelluric tensor analysis, *Geophys. J. Int.,* **159**(1), 69–82.

Ben-Itzhak, L.L. & Gvirtzman, H., 2005. Groundwater flow along and across structural folding: an example from the Judean desert, Israel, *J. Hydrol.,* **312,** 51–69.

Cagniard, L., 1953. Basic theory of the magneto-telluric method of geophysical prospecting, *Geophysics,* **18,** 605–635.

Constable, S., 2010. Ten years of marine CSEM for hydrocarbon exploration, *Geophysics,* **75**(5), 75A67–75A81.

Egbert, G.D., 1997. Robust multiple-station magnetotelluric data processing, *Geophys. J. Int.,* **130,** 475–496.

Eraifej, N., 2006. Gas geochemistry and isotopic signatures in the deep thermal waters in Jordan, *PhD thesis,* Technical University Freiberg.

Ezersky, M., Legchenko, A., Al-Zoubi, A., Levi, E., Akkawi, E. & Chalikakis, K., 2011. TEM study of the geoelectrical structure and groundwater salinity of the Nahal Hever sinkhole site, Dead Sea shore, Israel, *J. appl. Geophys.,* **75**(1), 99–112.

Fleischer, E., Goldberg, M., Gat, J. & Magaritz, M., 1977. Isotopic composition of formation waters from deep drillings in southern Israel, *Geochim. Cosmochim. Acta,* **41**(4), 511–525.

Gamble, T.D., Goubau, W.M. & Clarke, J., 1979. Magnetotellurics with a remote magnetic reference, *Geophysics,* **44**(1), 53–68.

Garfunkel, Z., 1981. Internal structure of the Dead Sea leaky transform (rift) in relation to plate kinematics, *Tectonophysics,* **80**(1–4), 81–108.

Garfunkel, Z. & Ben-Avraham, Z., 1996. The structure of the Dead Sea Basin, *Tectonophysics,* **266**(1-4), 155–176.

Garfunkel, Z., Zak, I. & Freund, R., 1981. Active faulting in the Dead Sea rift, *Tectonophysics,* **80**(1–4), 1–26.

Gilboa, Y., Fligelman, H. & Derin, B., 1993. Zohar-Kidod-Haqanaim fields—Israel Eastern Mediterranean basin, in Structural Traps, vol. 8, Treatise of Petroleum Geology Atlas of Oil and Gas Fields, eds. N. H. Foster and E. A. Beaumont, pp. 129–152, Am. Assoc. of Pet. Geol., Tulsa, OK, USA.

Gvirtzman, H. & Stanislavsky, E., 2000. Palaeohydrology of hydrocarbon maturation, migration and accumulation in the Dead Sea rift, *Basin Res.,* **12**(1), 79–93.

Gvirtzman, Z., 2004. Chronostratigraphic table and subsidence curves of southern Israel, *Isr. J. Earth Sci.,* **53**(1), 48–61.

Jiracek, G.R., 1990. Near-surface and topographic distortion in electromagnetic induction, *Surv. Geophys.,* **11,** 163–203.

Kafri, U. & Goldman, M., 2005. The use of the time domain electromagnetic method to delineate saline groundwater in granular and carbonate aquifers and to evaluate their porosity, *J. appl. Geophys.,* **57**(3), 167–178.

Kafri, U., Goldman, M. & Lang, B., 1997. Detection of subsurface brines, freshwater bodies and the interface configuration in-between by the time domain electromagnetic method in the Dead Sea rift, Israel, *Environ. Geol.,* **31,** 42–49.

Keller, V.G., 1988. Physical laws, electromagnetic induction and rock properties, in *Electromagnetic Methods in Applied Geophysics,* Chap. 2, pp. 13–51, ed. Nabighian, M.N., Society of Exploration Geophysics (SEG).

Khalil, B., 1992. *The geology of the Ar Rabba area, Geological Map Bulletin No. 22, Natural Resource Authority (Jordan),* Amman, Jordan.

Krings, T., 2007. The influence of robust statistics, remote reference, and horizontal magnetic transfer functions on data processing in magnetotellurics, *Master's thesis,* Institut für Geophysik Westfälische Wilhelms-Universität Münster and GeoForschungsZentrum Potsdam.

Levi, E., Goldman, M., Hadad, A. & Gvirtzman, H., 2008. Spatial delineation of groundwater salinity using deep time domain electromagnetic geophysical measurements: a feasibility study, *Water Resour. Res.,* **44**(12), W12404.

Masri, A., 2003. *The geology of Dhiban (Wadi Al Mujib) area, Geological Map Bulletin No. 54, Natural Resource Authority (Jordan),* Amman, Jordan.

Mechie, J., Abu-Ayyash, K., Ben-Avraham, Z., El-Kelani, R., Qabbani, I., Weber, M. & Group, D., 2009. Crustal structure of the southern Dead Sea Basin derived from project desire wide-angle seismic data, *Geophys. J. Int.,* **178**(1), 457–478.

Meqbel, N.M.M., 2009. The electrical conductivity structure of the Dead Sea Basin derived from 2D and 3D inversion of magnetotelluric data, *PhD thesis,* Free University of Berlin, Germany.

Powell, J.H., 1988. *The geology of the Karak area Map Sheet no. 3152iii, Geology Directorate, Natural Resources Authority,* Amman-Jordan.

Powell, J.H. & Basem, K. Moh'd., 2011. Evolution of Cretaceous to Eocene alluvial and carbonate platform sequences in central and south Jordan, *GeoArabia,* **16**(4), 29–82.

Rhoades, J., Chanduvi, F. & Lesch, S., 1999. *Soil Salinity Assessment: Methods and Interpretation of Electrical Conductivity Measurements,* FAO Irrigation and Drainage paper, Food and Agriculture Organization of the United Nations.

Ritter, O., Junge, A. & Dawes, G.J.K., 1998. New equipment and processing for magnetotelluric remote reference observations, *Geophys. J. Int.,* **132,** 535–548.

Ritter, O., Ryberg, T., Weckmann, U., Hoffmann-Rothe, A., Abueladas, A., Garfunkel, Z. & Group, D., 2003. Geophysical images of the Dead Sea transform in Jordan reveal an impermeable barrier for fluid flow, *Geophys. Res. Lett.,* **30**(14), 1741–1744.

Rodi, W. & Mackie, R.L., 2001. Nonlinear conjugate gradients algorithm for 2-D magnetotelluric inversion, *Geophysics,* **66**(1), 174–187.

Salameh, E. & El-Naser, H., 2000. The interface configuration of the fresh-/Dead Sea water—theory and measurements, *Acta Hydrochim. Hydrobiol.,* **28**(6), 323–328.

Salameh, E. & Hammouri, R., 2008. Sources of groundwater salinity along the flow path, Disi-Dead Sea/Jordan, *Environ. Geol.,* **55,** 1039–1053.

Shalev, E., Lyakhovsky, V. & Yechieli, Y., 2007. Is advective heat transport significant at the Dead Sea Basin? *Geofluids,* **7**(3), 292–300.

Stanislavsky, E. & Gvirtzman, H., 1999. Basin-scale migration of continental-rift brines: paleohydrologic modeling of the Dead Sea Basin, *Geology,* **27**(9), 791–794.

Telford, W.M., Geldart, L.P. & Sheriff, R.E., 1990. *Applied Geophysics,* 2nd Edn, Cambridge University Press, Cambridge.

Vozoff, K., 1972. The magnetotelluric method in the exploration of sedimentary basins, *Geophysics,* **37**(1), 98–141.

Weaver, J.T., 1994. *Mathematical Methods for Geo-electromagnetic Induction,* Applied and Engineering Mathematic Series, Research Studies Press, Taunton, Somerset, England.

Weckmann, U., Magunia, A. & Ritter, O., 2005. Effective noise separation for magnetotelluric single site data processing using a frequency domain selection scheme, *Geophys. J. Int.,* **161,** 635–652.

Yechieli, Y., Kafri, U., Goldman, M. & Voss, C., 2001. Factors controlling the configuration of the fresh/saline water interface in the Dead Sea coastal aquifers: synthesis of TDEM surveys and numerical groundwater modeling, *Hydrogeol. J.,* **9,** 367–377.

Yechieli, Y., 2006. The response of the groundwater system to changes in the Dead Sea level, in *New Frontiers in Dead Sea Paleoenvironmental Research,* No. 401 in Special paper of Geological Society of America, pp. 113–126, eds Enzel, Y., Agnon, A. & Stein, M., Geological Society of America.